RSC Advances

PAPER

View Article Online
View Journal | View Issue

Cite this: *RSC Adv.*, 2021, **11**, 34048

Two-dimensional polarized $MoTe_2$/GeS heterojunction with an intrinsic electric field for photocatalytic water-splitting†

Di Gu,[ab] Xiaoma Tao,[b] Hongmei Chen,[b] Yifang Ouyang,[*b] Weiling Zhu*[a] and Yong Du[c]

The construction of van der Waals heterostructures based on 2D polarized materials is a unique technique to achieve enhanced photocatalytic performance. We have investigated the intrinsic electric field and photocatalytic properties of the $MoTe_2$/GeS heterostructure *via* first-principles calculations. The results showed that a dipole-induced electric field induced by the GeS monolayer and an interface-induced electric field induced by the interface between the GeS monolayer and the $MoTe_2$ monolayer emerge in the 2D polarized $MoTe_2$/GeS heterostructure. The dipole-induced electric field contributes mainly to the total intrinsic electric field. Moreover, the 2D polarized $MoTe_2$/GeS heterostructure possesses many excellent and distinguished photocatalytic performance parameters, such as a direct semiconductor bandgap of 1.524 eV, a wide light spectrum ranging from the ultraviolet to near-infrared region with a high absorption coefficient (about 10^6 cm^{-1}), a total intrinsic electric field, which reduces the probability of the recombination of photo-generated electron–hole pairs effectively, and a suitable band alignment for the water-splitting reaction. These indicate that the 2D polarized $MoTe_2$/GeS van der Waals heterostructure is a potential novel high-efficient photocatalyst for water-splitting.

Received 1st August 2021
Accepted 29th September 2021

DOI: 10.1039/d1ra05840a

rsc.li/rsc-advances

1. Introduction

Due to the continuous high consumption of fossil fuels, humans have been facing energy crisis and the serial effects of environmental pollution.[1–4] Therefore, many fossil fuels should be replaced by renewable and clean energy, such as solar energy. Photocatalytic water splitting is an attractive technology that converts solar energy into hydrogen energy and possesses some unique advantages, such as the consumption of only solar energy instead of fossil fuels. Moreover, O_2 and H_2 can be obtained continuously under solar light. Lastly, this technology is clean and does not pollute the environment.[5–8] Therefore, this technology is considered a potential, feasible and efficient method to solve the environmental problems and the serious energy crisis at the same time.[9–11] Since Fujishima reported this technology for the first time in 1972,[12] photocatalytic water splitting has attracted a lot of attention around the world. Many materials, such as TiO_2 (ref. 13–17) and $SrTiO_3$,[18–20] have been reported as potential catalysts in this process. However, the efficiency of common materials in converting solar energy into hydrogen energy is still unsatisfactory and low, owing to their low solar-light-absorption efficiency and high carrier recombination rates.[21–24] In the process of solar energy to hydrogen energy conversion, solar-light absorption and carrier separation are the most important factors to improving the conversion efficiency. Moreover, the band alignments of catalysts should agree well with the redox potential; that is, the oxidation potential should be higher than the valence band maximum (VBM), and the reduction potential should be lower than the conduction band minimum (CBM) at the same time for the reaction of water splitting. However, these criteria are hardly met simultaneously due to the interaction between them.[25]

Recently, some researches have revealed that two-dimensional (2D) polarized materials, which possess a vertical intrinsic electric field induced by the dipole moment, show promising excellent properties for photocatalytic water splitting.[26–30] On the one hand, the carriers can be transferred from the interior to the surface efficiently under the effect of the induced vertical intrinsic electric field. On the other hand, effective solar-light harvesting can be realized. Therefore, 2D polarized materials possess potential properties that satisfy the demands of simultaneous solar-light absorption and carrier separation necessary for photocatalytic water splitting. Many two-dimensional polarized materials have been reported as potential and effective photocatalysts for producing hydrogen energy based on theoretical and experimental findings.[31–37] For

[a]*Department of Physics, School of Science, Guangdong University of Petrochemical Technology, Maoming, Guangdong 525000, People's Republic of China. E-mail: zhuweiling@gdupt.edu.cn*

[b]*School of Physical Science and Technology, Guangxi University, Nanning 530004, People's Republic of China. E-mail: ouyangyf@gxu.edu.cn*

[c]*State Key Laboratory of Powder Metallurgy, Central South University, Changsha, 410083, China*

† Electronic supplementary information (ESI) available. See DOI: 10.1039/d1ra05840a

instance, Yang *et al.* theoretically demonstrated that two-dimensional In_2Te_3, in which intrinsic electric field was experimentally attainable, can accomplish enhanced photocatalytic efficiency. Moreover, the theoretical efficiency even reached 32.1% on using the full solar spectrum.[38] In our previous study, the dipole of monolayer GeSe and monolayer GeS has been demonstrated as a unique photocatalyst for water splitting owing to the dipole-induced electric field.[39] Li *et al.* experimentally confirmed that GaN nanorod arrays possessed a distinguished advantage for charge separation due to the co-exposure of the polar and nonpolar surfaces, which induce an intrinsic electric field in the surface region. The charge-separation efficiency of the GaN nanorod arrays was 80%, which is much higher than the value (about 8%) of the GaN thin-film. Moreover, the quantum efficiency enhanced dramatically from 0.9% for the GaN thin-film to 6.9% for the GaN nanorod arrays.[40] Zhang *et al.* also experimentally confirmed that multi-field coupling in $KNbO_3$ nanostructures could enhance its catalytic performance owing to the polarization-modulated built-in electric fields, which effectively separated excited electron/hole pairs. The photocurrent density enhanced obviously from 25% for the nanocube counterpart to 55% for the $KNbO_3$ nanosheets.[41]

van der Waals (vdW) heterojunctions based on two-dimensional materials can deliver better performance than isolated monolayers because the properties of isolated materials are complementary.[42–48] Therefore, combining the different advantageous properties of different 2D materials to form vdW heterojunctions is an effective method to attain high-efficiency photocatalysts for water splitting. Moreover, the built-in electric field induced by the interface can effectively separate the excited carriers and enhance the photocatalytic activity.[49–56] For example, Yuan and co-workers experimentally confirmed that the photocatalytic activity of 2D-2D MoS_2/CdS,[45] MoS_2/g-C_3N_4 (ref. 57) and black phosphorus/MoS_2 (ref. 58) could be enhanced by interface engineering, which allowed the charge carrier to be transferred and separated efficiently *via* abundant channels at the large 2D interfaces. Sun and co-workers experimentally reported that a 2D Janus heterojunction based on $ZnIn_2S_4$ and WO_3 was a superior *Z*-scheme photocatalyst; it was helpful in boosting the separation of carriers, optimizing the charge lifetime and enhancing charge dynamics due to the effect of the internal electric field *via* the W–S bonds.[59] Moreover, many theoretical studies, using the first-principles calculations method, have indicated that vdW heterojunctions, such as $MoTe_2$/SnS_2,[48] blue phosphorene/BSe,[43] BCN/C_2N,[46] MoS_2/ZnO[44] and C_2N/WS_2,[49] are potential high-efficiency photocatalysts for water splitting. All the studies demonstrate the important role of the internal electric field of the vdW heterojunction in enhancing photocatalytic performance. Furthermore, polarized heterojunctions constructed based on two-dimensional polarized materials have been reported to possess a built-in electric field combined with not only an interface-induced electric field, but also a dipole-induced electric field.[59–61] However, the effects of the dipole-induced electric field and interface-induced electric field in the vdW heterojunctions based on 2D polarized materials are not clear. It is very important to study and understand the coupling mechanism of the electric fields in 2D polarized vdW heterojunctions as it is key to designing highly efficient catalysts for photocatalytic water splitting.

In order to shed further light on universal strategies for constructing highly efficient 2D polarized vdW heterojunctions, we investigated the coupling effect of the dipole-induced electric field and interface-induced electric field in two-dimensional polarized materials, using $MoTe_2$/GeS as the representative. The photocatalytic activity of the $MoTe_2$/GeS vdW heterojunction was systematically investigated.

2. Computational methods

In this paper, all the calculations were performed using the Vienna *ab initio* simulation package (VASP);[62] the Perdew–Burke–Ernzerhof (PBE) functional of the generalized gradient approximation (GGA) was considered for the exchange-correlation energy;[63] the projector-augmented-wave (PAW) was used for electron–ion interactions;[64] the optB88 method[65,66] was adopted for the long-range vdW interactions of the $MoTe_2$/GeS vdW heterojunction. To get a more accurate value, the bandgap was calculated by using the HSE06 hybrid functional.[67] The energy cut-off was set to 500 eV for the plane-wave expansion of the wave function. To relax all the structures fully, the Hellmann Feynman force convergence and the energy convergence were set to 0.001 eV $Å^{-1}$ and 10^{-6} eV, respectively. In order to exclude the artificial interactions, the thickness of the vacuum region was set to more than 20 Å along the *Z* direction. The gamma center schemes of $8 \times 8 \times 1$ and $11 \times 11 \times 1$ were used to sample the first Brillouin zone integration[68] for geometry relaxation and static calculations, respectively.

The energy alignment of the $MoTe_2$/GeS vdW heterojunction was calculated according to the method reported for polarized materials;[26,28,38] the VBM energy level was obtained by the following equation:

$$E_{VBM} = \varphi(\infty) - E_F \quad (1)$$

in which the electrostatic potential in a vacuum is represented by $\varphi(\infty)$, and the Fermi energy level corresponds to E_F. The CBM energy level was calculated in accordance with the following equation:

$$E_{CBM} = E_{VBM} + E_{gap} \quad (2)$$

where E_{gap} is the bandgap calculated by the HSE06 hybrid functional. The dielectric function was calculated according to eqn (3) to obtain the absorption spectrum.[69–71]

$$\alpha(\omega) = \sqrt{2}\omega\left(\sqrt{\varepsilon_1(\omega)^2 + \varepsilon_2(\omega)^2} - \varepsilon_1(\omega)\right)^{1/2} \quad (3)$$

in which $\alpha(\omega)$ is the absorption coefficient, and $\varepsilon_1(\omega)$ and $\varepsilon_2(\omega)$ are the real and imaginary parts of the frequency-dependent complex dielectric function, respectively.

3. Results and discussion

3.1 Structure of the $MoTe_2$/GeS vdW heterojunction

In order to construct the 2D polarized $MoTe_2$/GeS vdW heterojunction, the GeS monolayer and $MoTe_2$ monolayer were fully

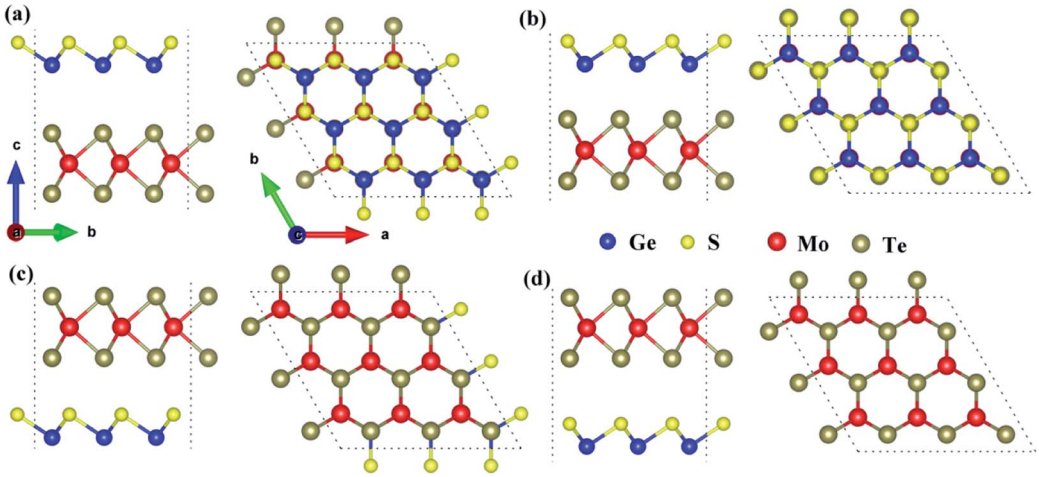

Fig. 1 Four prototype stacking structures of the $MoTe_2$/GeS heterojunctions: (a)–(d) side and top views of A1-, A2-, B1- and B2-stackings, respectively.

optimized first. The optimized lattice constants of the GeS monolayer and the $MoTe_2$ monolayer were 3.495 Å and 3.550 Å, respectively, which were consistent with previous studies.[39,72,73] It can be seen that the lattice mismatch, which was calculated from the difference in lattice constants between the GeS monolayer and the $MoTe_2$ monolayer, was about 1.5%. The lattice mismatch was in an acceptable range, indicating that it was possible to form a vertical vdW heterojunction along the *Z*-axis between the GeS monolayer and the $MoTe_2$ monolayer. As shown in Fig. 1, four possible stackings were considered, namely A1-, A2- and B1-, B2-stackings, to form the 2D polarized $MoTe_2$/GeS vdW heterojunction. In the A1- and A2-stackings, the heterojunctions were formed based on the Ge–Te interface, in which the Ge atomic surface of the GeS monolayer approached the Te atomic surface of the $MoTe_2$ monolayer. In contrast, the heterojunctions of the B1- and B2-stackings were formed based on the S–Te interface, in which the S atomic surface of the GeS monolayer approached the Te atomic surface of the $MoTe_2$ monolayer. To obtain a stable heterojunction, all four stackings were fully optimized. The relationship between the lattice constant and the total energy of the $MoTe_2$/GeS vdW heterojunction was calculated. As shown in Fig. S1,† the energy of the $MoTe_2$/GeS vdW heterojunction was varied as the lattice constant was tuned, and the minimum value indicated the most stable structure. Therefore, in order to analyse the differences among the four stacking prototypes, the lattice constants were all taken as 3.554 Å.

3.2 The total intrinsic electric field of the $MoTe_2$/GeS heterojunction

Because the electronegativities of atoms are different in two-dimensional polarized materials, the dipole-induced electric field induced by the GeS monolayer and the interface-induced electric field induced by the interface between GeS monolayer and $MoTe_2$ monolayer emerged in the 2D polarized $MoTe_2$/GeS vdW heterojunction. The total intrinsic electric field was composed of the dipole-induced electric field and the interface-induced electric field. As shown in Fig. 2, A2-stacking and B2-stacking were used as the models to study the coupling effect between the dipole-induced electric field and interface-induced electric field in the polarized $MoTe_2$/GeS vdW heterojunction. The dipole-induced electric fields in all the stacking orders were almost the same because they were induced by the same GeS monolayer, and the electric fields were along the *Z* direction. In contrast, the isolated $MoTe_2$ layer did not possess a similar electric field due to the symmetrical structure of the monolayer. When the GeS monolayer and the $MoTe_2$ monolayer were stacked vertically to form the $MoTe_2$/GeS vdW heterojunction, two different interfaces (the Ge–Te interface and the S–Te interface) were considered because of the electric field in the GeS monolayer along the *Z* direction. Both the atomic interfaces were not symmetrical, indicating that a new intrinsic dipole would be induced due to the different electronegativity values of the two atoms. Therefore, there would be an interface-induced electric field through the Ge–Te interface or the S–Te interface in the polarized $MoTe_2$/GeS vdW heterojunction. Moreover,

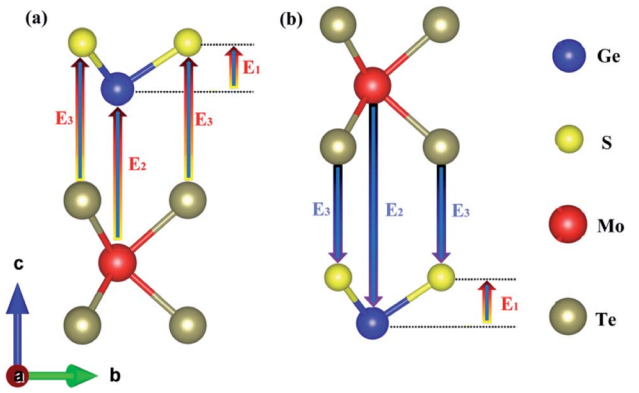

Fig. 2 The coupling of the dipole-induced electric field and the interface-induced electric field in the polarized $MoTe_2$/GeS vdW heterojunction based on (a) the Ge–Te interface and (b) the S–Te interface.

since the electric field is closely related to the interlayer distance, only the atoms in contact with each other were considered. The total intrinsic electric field E in the two-dimensional polarized vdW heterojunction can be expressed as:

$$E = E_{\mathrm{p}} + E_i \tag{4}$$

in which E_{p} is the dipole-induced electric field, and E_i is the interface-induced electric field. There was no electric field in the isolated $MoTe_2$ layer, and the dipole-induced electric field of heterojunction was only contributed by the GeS layer (represented by E_1); therefore, it is obvious that E_{p} was equal to E_1. In contrast, the interface-induced electric field in the Ge–Te interface was different from that in the S–Te interface due to the difference in the electronegativity of the atoms. For example, the electronegativity of the Mo atom is greater than the electronegativity of the Ge atom, which would induce a built-in electric field at the interface, in the direction from the Mo-atom layer to the Ge-atom layer (represented by E_2). Similarly, the electronegativity of the Te atom is greater than that of the S atom, inducing a built-in electric field at the interface, in the direction from the Te atomic layer to the S atomic layer (represented by E_3). Therefore, E_i can be expressed as the vectorial sum of E_2 and E_3.

In this paper, the Z-axis was selected as the positive direction; then, the total intrinsic electric field (E_{A}) of the polarized $MoTe_2$/GeS vdW heterojunction based on the Ge–Te interface (A-stacking) was expressed as the vectorial sum of E_1, E_2 and E_3. Similarly, the total intrinsic electric field (E_{B}) of the polarized $MoTe_2$/GeS vdW heterojunction based on the Ge–Te interface (the B-stacking) was expressed as the vectorial sum of E_1, E_2 and E_3. Significantly, in the B-stacking case, E_1 was in the opposite direction to E_2 and E_3. In addition, the built-in electric field E_{eff} was mainly induced by the intrinsic dipole P in accordance with the following formula:

$$E_{\mathrm{eff}} = \frac{P}{\varepsilon S d} \tag{5}$$

where the dielectric constant, surface area and distance between the atomic layers are expressed as ε, S and d, respectively. This indicates that the built-in electric field is inversely proportional to the distance d. The interlayer distance of GeS was small, and the atomic distance at the heterojunction interface was large, so E_i ($i = 2$ or 3) was much smaller than E_{p}. Therefore, the relationship between E_{A}, E_{B} and E_{p} was:

$$E_{\mathrm{B}} < E_{\mathrm{p}} < E_{\mathrm{A}} \tag{6}$$

This indicated that E_{A} and E_{B} were mainly contributed by E_{p} and that the vector directions of E_{A} and E_{B} were consistent with that of E_{p} along the positive direction of the Z-axis.

The electronegativity of atoms located in the upper surface and lower surface were different. Therefore, the built-in electric field E_{eff} and a surface electrostatic potential difference $\Delta\Phi$ were induced by the intrinsic dipole P between the upper and lower surfaces. E_{eff} and $\Delta\Phi$ are the intrinsic characteristics of polarized materials, which can result in the separation and migration of photo-generated carriers and reduce the recombination rate of carriers effectively, thus enhancing the photocatalytic performance of the two-dimensional polarized materials. The relationship between the built-in electric field E_{eff} and the surface electrostatic potential difference $\Delta\Phi$ can be expressed by the following formula:

$$\Delta\Phi = eE_{\mathrm{eff}}d \tag{7}$$

where the elementary charge constant is expressed as e, and d is the distance between the atomic layers. It can be seen that $\Delta\Phi$ is directly proportional to E_{eff}. The larger the surface electrostatic potential difference $\Delta\Phi$, the larger was the induced electric field E_{eff}. As shown in Fig. S2,† the planar average potential of the isolated GeS monolayer and the isolated $MoTe_2$ monolayer in the different stacking structures of the $MoTe_2$/GeS vdW heterojunction were calculated. For the isolated GeS monolayer, there was a significant surface potential difference $\Delta\Phi$, and the potential energy of the Ge atomic layer at the bottom was lower than the potential energy of the S atomic layer on the top, indicating that the direction of dipole-induced electric field (E_{p}) was pointing from the Ge-atom layer at the bottom to the S-atom layer at the top. For the isolated $MoTe_2$ monolayer, the potential energies of the upper and lower surfaces were equal, and the surface potential difference was 0 eV because both the upper and lower surfaces were symmetrical Te atomic layers with the same electronegativity. It was worth noting that the $\Delta\Phi$s of the isolated GeS monolayer in the A1-, A2- and B1-stackings was 1.082 eV, and the $\Delta\Phi$ of the isolated GeS monolayer in the B2 stacking was 1.083 eV. All of them were almost the same, and the difference between them was negligible. Therefore, this indicated that the dipole-induced electric field (E_1) of all the four differently stacked heterojunctions was the same since E_1 was induced only by the same isolated GeS layer.

The planar average potentials of the $MoTe_2$/GeS vdW heterojunction in the A1-, A2-, B1-, and B2-stacking configurations are shown in Fig. 3. All the stackings presented an obvious surface potential difference $\Delta\Phi$, and the potential energy at the bottom was lower than the potential energy at the top, indicating that the direction of the total intrinsic electric field (E) was along the Z direction, which is consistent with the direction of E_{p} of the GeS monolayer. Moreover, the interface-induced electric fields in the Ge–Te interfaces of the A1- and A2-stackings were different from those in the S–Te interfaces of the B1- and B2-stackings. However, the potential energy on the $MoTe_2$ side was lower than that on the GeS side in the A1-, A2-, B1- and B2-stackings. This indicated that the total electric field of the heterojunction was mainly contributed by the dipole-induced electric field, while the interface-induced electric field was weaker.

As shown in Fig. 3, the $\Delta\Phi$s of the $MoTe_2$/GeS vdW heterojunctions in the A1-, A2-, B1-, and B2-stackings were 1.106 eV, 1.177 eV, 1.036 eV, and 1.057 eV, respectively, while that of the isolated GeS monolayer was 1.082 eV. It indicated that the total electric field of the heterojunction was mainly contributed by the dipole-induced electric field and suggested that the dipole-induced electric field was much larger than the interface-induced electric field. Moreover, it was found that

$$\Delta\Phi(\mathrm{B}) < \Delta\Phi(\mathrm{GeS}) < \Delta\Phi(\mathrm{A}) \tag{8}$$

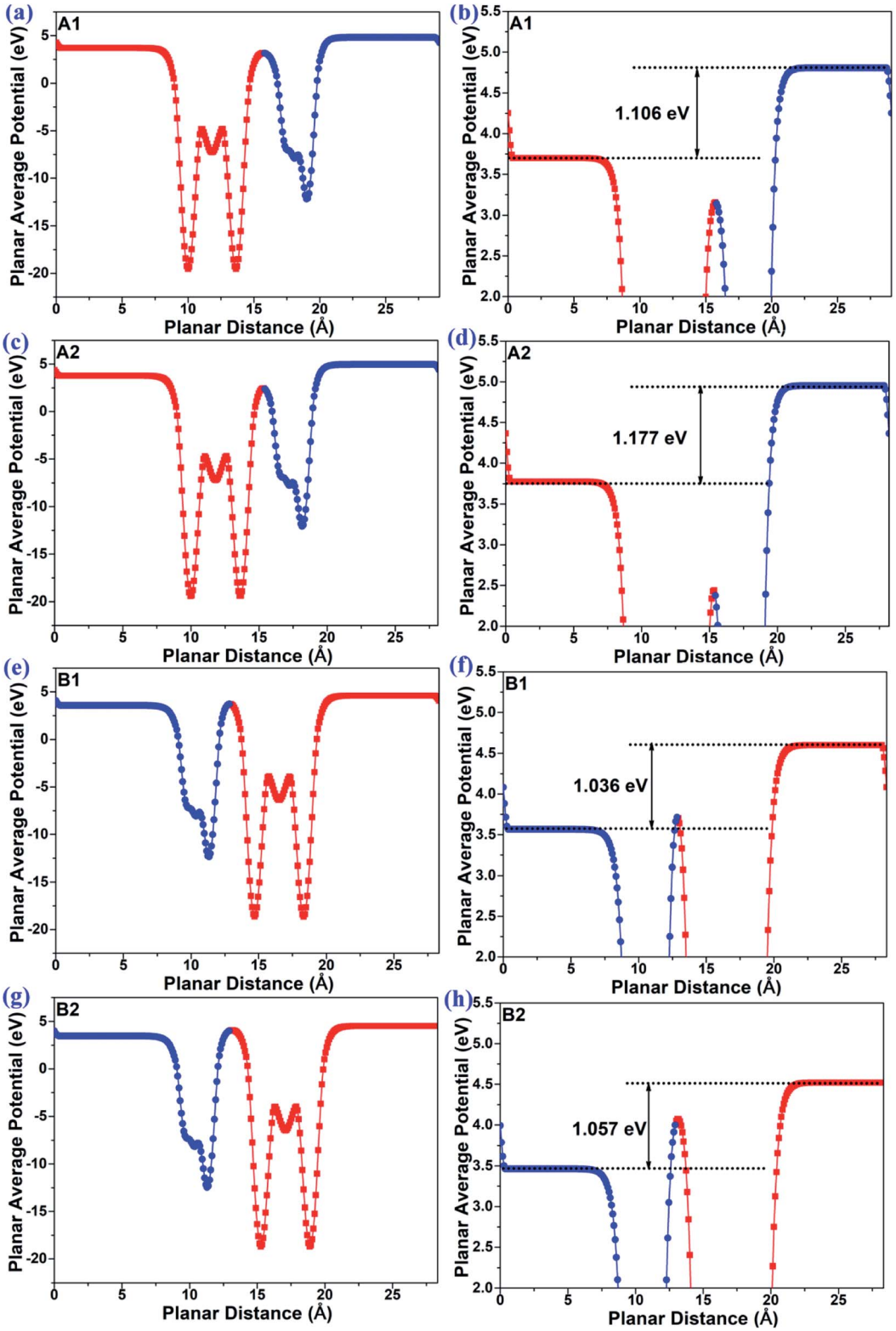

Fig. 3 The planar average potential of the $MoTe_2$/GeS vdW heterojunction in (a) and (b) A1-, (c) and (d) A2-, (e) and (f) B1- and (g) and (h) B2-stackings.

where $\Delta\Phi$(B) and $\Delta\Phi$(A) are, respectively, the surface potential differences of the B-type and A-type stacked heterojunctions, and $\Delta\Phi$(GeS) is the surface potential difference of the GeS monolayer. The surface potential difference of the B-type stacked heterojunction was smaller than that of the GeS monolayer, while the surface potential difference of the A-type

stacked heterojunction was larger compared with that of the GeS monolayer. This confirmed that the interface-induced electric field was different in the A-type and B-type stackings. In the A-type with the Ge–Te interface, the direction was along the Z direction, while in B-type with the S–Te interface, the direction was along the $-Z$ direction. These results agree well with the analysis in Fig. 2 mentioned above.

In order to provide insights into the mechanism of the interface-induced electric field, we calculated the planar average potential difference ΔP of the $MoTe_2$/GeS vdW heterojunction by the following formula:

$$\Delta P = P_{\text{heterostructure}} - P_{\text{GeS}} - P_{\text{MoTe}_2} \quad (9)$$

where $P_{\text{heterostructure}}$, P_{GeS} and P_{MoTe_2} are the planar average potentials of the $MoTe_2$/GeS vdW heterojunction, GeS monolayer and $MoTe_2$ monolayer, respectively. ΔP was mainly contributed by the interface-induced electric field, indicating that the direction of ΔP represented the direction of the interface-induced electric field. As shown in Fig. 4, for the A1- and A2-stackings based on the Ge–Te interface, the direction of ΔP was along the positive direction of the Z-axis, indicating that the interface-induced electric field was directed from the bottom atomic layer to the top atomic layer. By contrast, for the B1- and B2-stackings based on the S–Te interface, the direction of ΔP was along the negative direction of the Z-axis, which indicated the interface-induced electric field was directed from the top atomic layer to the bottom atomic layer. Therefore, the interface-induced electric field was closely related to the stacking order based on the different interface structures. The direction of the interface-induced electric field was the same for the stackings based on the same interfaces. The results were consistent with the above-mentioned analysis Fig. 2 and 3. Moreover, it was found that the value of the planar average potential difference (ΔP), which represents the interface-induced electric field induced by the interface between the GeS monolayer and the $MoTe_2$ monolayer, was much smaller than the value of the surface potential difference of the GeS monolayer ($\Delta\Phi$), which represents the dipole-induced electric field induced by the GeS monolayer. This confirmed that the total intrinsic electric field was mainly contributed by the dipole-induced electric field, while the interface-induced electric field contributed less to the total intrinsic electric field. Therefore, when the interface-induced electric field and the dipole-induced electric field are in the same direction, a larger total intrinsic electric field would be induced. Meanwhile, the total intrinsic electric field would be slightly smaller than the dipole-induced electric field when the interface-induced electric field and the dipole-induced electric field are in opposite directions.

3.3 Stability and phonon dispersion

The coupling mechanism of the built-in dipole electric field and the interface-induced electric field of the different stacking sequences has been studied above. The A2-stacking structure

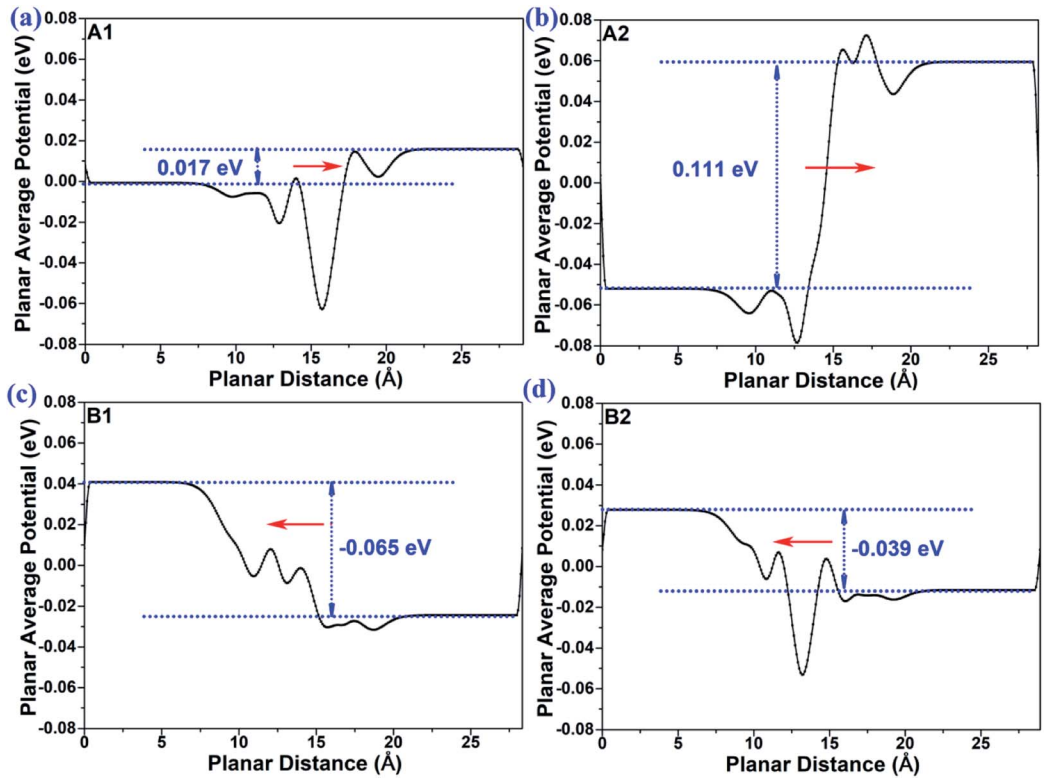

Fig. 4 The plane-average potential difference along the Z direction of $MoTe_2$/GeS vdW heterojunction for (a) A1-, (b) A2-, (c) B1- and (d) B2-stacking.

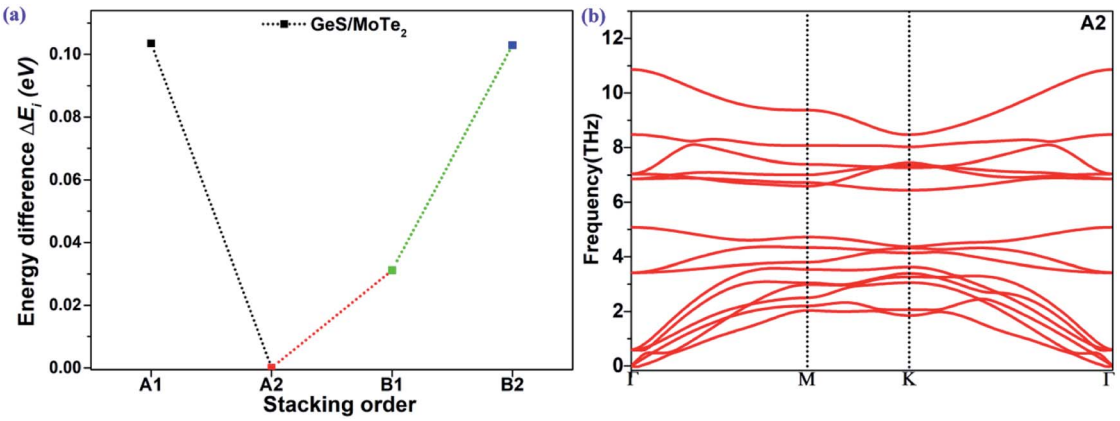

Fig. 5 (a) Energy difference ΔE_i (eV) between the optimized $MoTe_2$/GeS vdW heterojunctions and the most stable heterojunction; (b) the phonon spectrum of the $MoTe_2$/GeS vdW heterojunction.

possessed the largest total intrinsic electric field, which is useful to separate the photo-generated carriers, expand the solar light absorption region and enhance the performance of the photocatalytic water splitting. To obtain the most stable vdW heterojunction, all the four stacking structures were fully optimized, and the total energies of the different stacking structures were also calculated. As shown in Fig. 5(a), it was clear that the total energy of the A2-stacking was the minimum, while the B2- and A1-stackings possessed the maximum value, and the total energy of the B1-stacking was in between, indicating that the A2-stacking would be the most stable structure among the four. Therefore, the A2-stacking was taken as the optimum structure to discuss the properties of the $MoTe_2$/GeS vdW heterojunction. To verify the thermodynamic and dynamical stability of the $MoTe_2$/GeS vdW heterojunction, the binding energy E_d of the $MoTe_2$/GeS heterojunction was calculated by the following formula:

$$E_d = \frac{E_h - E_{GeS} - EMoTe_2}{A} \quad (10)$$

in which E_h, E_{MoTe_2} and E_{GeS} are the total energy corresponding to the $MoTe_2$/GeS vdW heterojunction, isolated $MoTe_2$ monolayer and isolated GeS monolayer, respectively. The interface area of the $MoTe_2$/GeS vdW heterojunction is represented as A. According to the definition, the vdW heterojunction structure

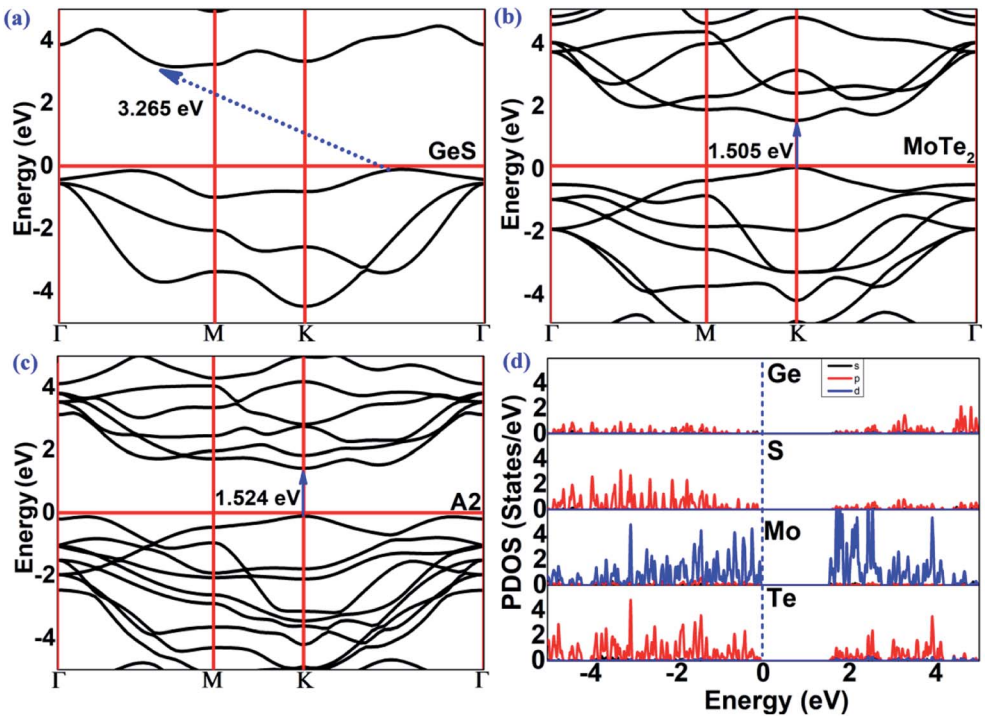

Fig. 6 The band structures (HSE06) of the (a) GeS monolayer, (b) $MoTe_2$ monolayer, (c) $MoTe_2$/GeS vdW heterojunction. (d) The partial density of states (PDOS) of the $MoTe_2$/GeS vdW heterojunction.

would be the most stable if the value of binding energy is the most negative. The value of binding energy of the $MoTe_2$/GeS vdW heterojunction was about -48.34 meV Å^{-2}, similar to those of other vdW heterojunctions.[70,74–76] This confirmed that the $MoTe_2$/GeS vdW heterojunction was thermodynamically stable. Moreover, the phonon spectrum of the vdW heterojunction with A2-stacking was calculated, as shown in Fig. 5(b); there was no obvious virtual frequency in the phonon spectrum, which confirmed its dynamical stability. Therefore, the A2-stacked vdW heterojunction was used as the representative to study the photocatalytic performance.

3.4 Electronic properties

The band structures of the GeS monolayer, $MoTe_2$ monolayer and $MoTe_2$/GeS vdW heterojunction were calculated using the HSE06 method to get accurate values. As shown in Fig. 6(a), for the GeS monolayer, the valence band maximum (VBM) was located between K and Γ. As a contrast, the conduction band minimum (CBM) was located between Γ and M. The GeS monolayer was an indirect semiconductor with a bandgap of 3.265 eV, which is very large and similar to traditional bulk material catalysts, such as TiO_2. This indicated that only a few ultraviolet light spectra, which is just about 5% of the full solar spectrum, would be absorbed and utilized by the GeS monolayer. Thus, the GeS monolayer possesses low solar-light absorption and low conversion efficiency in photocatalytic water splitting. As shown in Fig. 6(b), the $MoTe_2$ monolayer was a direct semiconductor with the CBM and VBM located at the K point. The bandgap of the $MoTe_2$ monolayer was 1.505 eV, which is consistent with previous results.[77] Compared with the GeS monolayer, the $MoTe_2$ monolayer possesses a direct semiconductor characteristic with a suitable value of bandgap for solar-light conversion and absorption of the visible light spectrum. This means that the $MoTe_2$ monolayer is a potential material for solar spectrum utilization. As shown in Fig. 6(c), the $MoTe_2$/GeS vdW heterojunction was also a direct semiconductor with the CBM and the VBM located at the K point. The bandgap of the $MoTe_2$/GeS vdW heterojunction was 1.524 eV. The band structure of the $MoTe_2$/GeS vdW heterojunction retained the individual band characteristics of the component monolayers. It was notable that the CBM and VBM were very similar to those of the $MoTe_2$ monolayer, and therefore, the $MoTe_2$/GeS vdW heterojunction maintained the direct bandgap semiconductor characteristics as the $MoTe_2$ monolayer. Moreover, since the smaller bandgap of the $MoTe_2$/GeS vdW heterojunction than that of the GeS monolayer suggested that light in a wider solar spectrum (including ultraviolet light and visible spectrum) would be absorbed effectively. Therefore, the construction of $MoTe_2$/GeS vdW heterojunction is an effective way to solve the problem of low solar-light absorption in the GeS monolayer.

The effective mass m^* of electrons and holes in the $MoTe_2$ monolayer, GeS monolayer and $MoTe_2$/GeS heterojunction were calculated by fitting the HSE06 band structures to a parabola, according to the following equation:

$$E = \frac{\hbar^2 k^2}{2m^*} \tag{11}$$

For the $MoTe_2$ monolayer, the CBM and VBM were always located in K point, and the effective electron and hole masses were $0.635m_e$ and $-0.752m_e$, which were consistent with the values $0.58m_e$ and $-0.74m_e$ reported in the previous studies.[78] Here, the electron static mass is represented as m_e. For the GeS monolayer, the VBM was located between K and Γ, and the CBM was located between Γ and M; the effective electron and hole masses were $1.518m_e$ and $-1.534m_e$, respectively. Moreover, for the $MoTe_2$/GeS vdW heterojunction, the CBM and VBM were always located at the K point, and the effective electron and hole masses were $0.723m_e$ and $-0.825m_e$, respectively. It was notable that the effective masses of electrons and holes in the $MoTe_2$/GeS vdW heterojunction were between those of the $MoTe_2$ monolayer and the GeS monolayer but closer to those of the $MoTe_2$ monolayer because the $MoTe_2$/GeS vdW heterojunction maintained the advantageous band structural characteristics of the $MoTe_2$ monolayer.

In order to see the contribution of each element to the band structure of the $MoTe_2$/GeS vdW heterojunction, the partial density of states (PDOS) of the $MoTe_2$/GeS vdW heterojunction was calculated, as shown in Fig. 6(d). The CBM was mainly contributed by the d orbitals of the Mo atoms and the p orbitals of the Te atoms. In contrast, the VBM was mainly contributed by the d electrons of the Mo atoms. Therefore, the direct bandgap semiconductor characteristics of the $MoTe_2$/GeS vdW heterojunction were mainly determined by the $MoTe_2$ monolayer, which was beneficial to improving the solar-light conversion and enhancing the performance in photocatalytic water splitting.

The two-dimensional polarized materials manifest promising and potential properties in the conversion process of solar energy to hydrogen energy, thanks to the effect of the vertical intrinsic electric field. Not only can the carriers be separated efficiently from the interior to the surface under the effect of the intrinsic electric field, but the bandgap is also effectively reduced to align with the redox potential of water, as required for photocatalytic water splitting. According to the mechanism of photocatalytic water splitting by two-dimensional polarized materials introduced by Yang's group,[26] under the effect of the intrinsic electric field, all the energies, including vacuum energy, reduction potential and oxidation potential, bend along the direction of the electric field. Therefore, the energy alignment of two-dimensional polarized materials is different from that of non-polarized 2D materials.

As shown in Fig. 7, the $MoTe_2$/GeS vdW heterojunction possesses an intrinsic electric field, which is a combination of the dipole-induced electric field and the interface-induced electric field at the heterojunction. The intrinsic electric field is along the Z direction, therefore the energy, including the vacuum energy, the reduction potential and the oxidation potential, bends along the direction of the electric field. It is obvious that the surface potential difference $\Delta\Phi = 1.177$ eV is very helpful to separate the photo-general carriers from the interior to the surface efficiently. Under the effect of the intrinsic electric field, the electrons quickly migrate to the bottom layer of the heterojunction, while the holes migrate to the top layer of the heterojunction. At the top layer of the heterojunction, the VBM energy level is lower than the oxidation

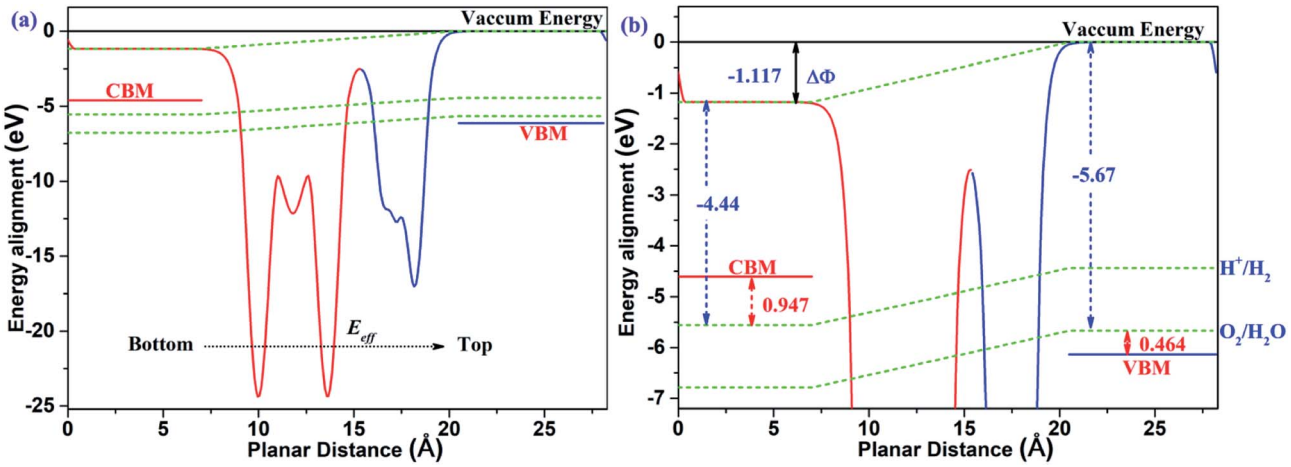

Fig. 7 (a) The energy alignment of the $MoTe_2$/GeS vdW heterojunction; (b) an enlarged section of (a).

potential of O_2/H_2O (−5.67 eV). The energy difference (ΔE_v) between the oxidation potential and the VBM energy level is 0.464 eV, which drives water to generate oxygen and H^+ under the action of holes according to the following equation.

$$4h^+ + 2H_2O \rightarrow O_2 + 4H^+ \quad (12)$$

In contrast, at the bottom layer of the heterojunction, the CBM energy level is higher compared with the reduction potential of H^+/H_2 (−4.44 eV). The energy difference (ΔE_c) between the reduction potential and the CBM energy level is 0.947 eV, driving water to generate hydrogen and OH^- under the action of electrons according to the following equation.

$$4e^- + 4H_2O \rightarrow 2H_2 + 4OH^- \quad (13)$$

Moreover, both ΔE_v and ΔE_c are suitable for the harmonious reaction. These results indicate that the heterojunction would be a potential and effective photocatalyst for producing hydrogen and oxygen due to the advantages of the intrinsic electric field.

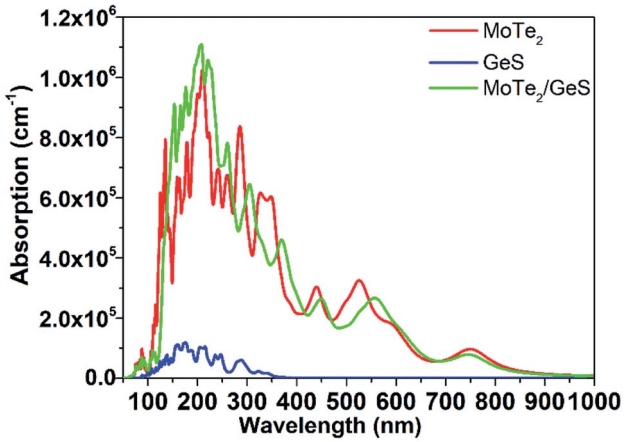

Fig. 8 Absorption coefficients of the GeS monolayer, $MoTe_2$ monolayer, and $MoTe_2$/GeS vdW heterojunction.

3.5 Optical properties

It is known that solar-light absorption is the first and the most important step during the process of solar energy to hydrogen energy conversion. In order to study the absorption performance of the $MoTe_2$/GeS vdW heterojunction, the dielectric function was calculated to obtain the absorption spectrum.[69–71] The absorption spectra of the GeS monolayer, $MoTe_2$ monolayer and $MoTe_2$/GeS vdW heterojunction are shown in Fig. 8. It was obvious that the absorption performance of the GeS monolayer was unsatisfactory, involving only the ultraviolet region, which is just about 5% of the solar spectrum. Meanwhile, the visible and infrared regions, which form the most part (about 95%) of the solar spectrum, would not be absorbed efficiently because the bandgap of the GeS monolayer was larger than 3.0 eV. In contrast, the $MoTe_2$ monolayer possessed excellent and distinguishable absorption performance as the $MoTe_2$ monolayer was a direct semiconductor with a suitable bandgap to aid the absorption of a wider range of solar light, including the ultraviolet region (<400 nm) and the visible region (400–800 nm). Moreover, the $MoTe_2$ monolayer had a strong light-absorption capacity, and its absorption coefficient could reach 10^6 cm^{-1}. The absorption performance of the $MoTe_2$/GeS vdW heterojunction was better than the GeS monolayer as it was mainly determined by the $MoTe_2$ monolayer. Both the ultraviolet spectrum region (<400 nm) and the visible spectrum region (400–800 nm) were absorbed by the $MoTe_2$/GeS vdW heterojunction. Moreover, the absorption coefficient of the $MoTe_2$/GeS vdW heterojunction was about 10^6 cm^{-1}, indicating excellent and distinguished absorption performance as that of the $MoTe_2$ monolayer. Therefore, the construction of the $MoTe_2$/GeS vdW heterojunction was helpful toward enhancing the conversion efficiency of solar energy and improving the efficiency of photocatalytic water splitting under a wide light spectrum.

4. Conclusion

In summary, we have constructed a $MoTe_2$/GeS vdW heterojunction based on two-dimensional polarized materials and systematically investigated the coupling effect of the dipole-

induced electric field and interface-induced electric field on the photocatalytic activity *via* first-principles calculations. The results indicate that a dipole-induced electric field, which is induced by the GeS monolayer, and an interface-induced electric field, which is induced by the interface between the GeS monolayer and the $MoTe_2$ monolayer, emerge in the 2D polarized $MoTe_2$/GeS vdW heterojunction. The total intrinsic electric field was composed of the dipole-induced electric field and the interface-induced electric field. The dipole-induced electric field was much larger compared to the interface-induced electric field, indicating the dominant contribution of the former to the total intrinsic electric field. Moreover, our results indicate that the two-dimensional polarized $MoTe_2$/GeS vdW heterojunction is a potential efficient photocatalyst for producing hydrogen energy due to the following reasons. The $MoTe_2$/GeS vdW heterojunction is a direct semiconductor with a bandgap of about 1.524 eV, which is very useful for optoelectronic and photocatalytic applications. Moreover, the $MoTe_2$/GeS vdW heterojunction possesses excellent solar absorption performance in a wide light spectrum and presents a high absorption coefficient (about 10^6 cm^{-1}). The $MoTe_2$/GeS vdW heterojunction possesses a total intrinsic electric field, which is the combination of the dipole-induced electric field and the interface-induced electric field. The intrinsic electric field is helpful in effectively reducing the recombination rate of the electron–hole pairs. The band alignments of the $MoTe_2$/GeS vdW heterojunction satisfy the redox potential very well. On the whole, the two-dimensional polarized material-based $MoTe_2$/GeS vdW heterojunction would be a highly efficient photocatalyst for producing hydrogen energy under ultraviolet to near-infrared light. Our study may shed light on a strategy for building highly efficient 2D polarized vdW heterojunctions for water splitting under the full solar light spectrum.

Data availability

The data that support the findings of this study are available from the corresponding author upon reasonable request.

Author contributions

Di Gu: data curation, formal analysis, conceptualization, investigation, validation, visualization, writing – original draft. Xiaoma Tao: data curation, methodology. Hongmei Chen: visualization, conceptualization. Yifang Ouyang: funding acquisition, project administration, supervision, writing – review & editing. Weiling Zhu: software, supervision, validation, resources. Yong Du: conceptualization.

Conflicts of interest

The authors declare that they have no known competing financial interests or personal relationships that could have appeared to influence the work reported in this paper.

Acknowledgements

Authors acknowledge the financial support from National Natural Science Foundation of China (11964003), Projects of PhDs' Start-up Research of GDUPT (2020bs008) and the Guangxi Natural Science Foundation (2018GXNSFAA281291, 2019GXNSFAA185058).

References

1 W. Lubitz and W. Tumas, *Chem. Rev.*, 2007, **107**, 3900–3903.
2 P. Kumar, R. Boukherroub and K. Shankar, *J. Mater. Chem. A*, 2018, **6**, 12876–12931.
3 A. J. Esswein and D. G. Nocera, *Chem. Rev.*, 2007, **107**, 4022–4047.
4 T. m. Su, Z. z. Qin, H. b. Ji and Z. Wu, *Nanotechnology*, 2019, **30**, 502002.
5 M. Ni, M. K. H. Leung, D. Y. C. Leung and K. Sumathy, *Renewable Sustainable Energy Rev.*, 2007, **11**, 401–425.
6 J. Ran, J. Zhang, J. Yu, M. Jaroniec and S. Z. Qiao, *Chem. Soc. Rev.*, 2014, **43**, 7787–7812.
7 C. Acar, I. Dincer and G. F. Naterer, *Int. J. Energy Res.*, 2016, **40**, 1449–1473.
8 Y. g. Li, Y. L. Li, B. s. Sa and R. Ahuja, *Catal. Sci. Technol.*, 2017, **7**, 545–559.
9 K. Zhang and L. Guo, *Catal. Sci. Technol.*, 2013, **3**, 1672.
10 K. M. Lee, C. W. Lai, K. S. Ngai and J. C. Juan, *Water Res.*, 2016, **88**, 428–448.
11 N. Xiao, S. Li, X. Li, L. Ge, Y. Gao and N. Li, *Chin. J. Catal.*, 2020, **41**, 642–671.
12 A. Fujishima and K. Honda, *Nature*, 1972, **238**, 37–38.
13 R. Asahi, T. Morikawa, T. Ohwaki, K. Aoki and Y. Taga, *Science*, 2001, **293**, 269–271.
14 W. Choi, A. Termin and M. R. Hoffmann, *J. Phys. Chem.*, 1994, **98**, 13669–13679.
15 U. Diebold, *Surf. Sci. Rep.*, 2003, **48**, 53–229.
16 T. Maric, M. Z. M. Nasir, R. D. Webster and M. Pumera, *Adv. Funct. Mater.*, 2020, **30**, 1908614.
17 H. G. Yang, C. H. Sun, S. Z. Qiao, J. Zou, G. Liu, S. C. Smith, H. M. Cheng and G. Q. Lu, *Nature*, 2008, **453**, 638–641.
18 T. K. Townsend, N. D. Browning and F. E. Osterloh, *ACS Nano*, 2012, **6**, 7420–7426.
19 K. Domen, A. Kudo and T. Onishi, *J. Catal.*, 1986, **102**, 92–98.
20 K. Domen, S. Naito, T. Onishi and K. Tamaru, *Chem. Phys. Lett.*, 1982, **92**, 433–434.
21 H. z. Luo, Z. t. Zeng, G. m. Zeng, C. Zhang, R. Xiao, D. Huang, C. Lai, M. Cheng, W. Wang, W. Xiong, Y. Yang, L. Qin, C. Zhou, H. Wang, Y. Zhou and S. Tian, *Chem. Eng. J.*, 2020, **383**, 123196.
22 J. b. Pan, S. Shen, W. Zhou, J. Tang, H. z. Ding, J. b. Wang, L. Chen, C.-T. Au and S.-F. Yin, *Acta Phys.-Chim. Sin.*, 2020, **36**, 1905068.
23 M. Xiao, B. Luo, Z. Wang, S. Wang and L. Wang, *Sol. RRL*, 2020, **4**, 1900509.
24 J. Liu, Y. Liu, N. Y. Liu, Y. Han, X. Zhang, H. Huang, Y. Lifshitz, S. T. Lee, J. Zhong and Z. Kang, *Science*, 2015, **347**, 970–974.

25 C. F. Fu, X. Wu and J. Yang, *Adv. Mater.*, 2018, **30**, 1802106.
26 X. X. Li, Z. Y. Li and J. L. Yang, *Phys. Rev. Lett.*, 2014, **112**, 018301.
27 Y. Ji, M. Yang, H. Dong, T. Hou, L. Wang and Y. Li, *Nanoscale*, 2017, **9**, 8608–8615.
28 C. F. Fu, X. x. Li, Q. q. Luo and J. Yang, *J. Mater. Chem. A*, 2017, **5**, 24972–24980.
29 J. Yun, Y. Zhang, Y. Ren, P. Kang, J. Yan, W. Zhao, Z. Zhang and H. Guo, *Sol. Energy Mater. Sol. Cells*, 2020, **210**, 110516.
30 P. T. Huong, M. Idrees, B. Amin, N. N. Hieu, H. V. Phuc, L. T. Hoa and C. V. Nguyen, *RSC Adv.*, 2020, **10**, 24127–24133.
31 C. x. Xia, W. q. Xiong, J. Du, T. Wang, Y. Peng and J. Li, *Phys. Rev. B: Condens. Matter Mater. Phys.*, 2018, **98**, 165424.
32 Y. Li, J. J. Wang, B. Z. Zhou, F. Wang, Y. Miao, J. Wei, B. Zhang and K. Zhang, *Phys. Chem. Chem. Phys.*, 2018, **20**, 24109–24116.
33 A. C. RiisJensen, M. Pandey and K. S. Thygesen, *J. Phys. Chem. C*, 2018, **122**, 24520–24526.
34 Y. j. Ji, M. y. Yang, H. p. Lin, T. Hou, L. Wang, Y. Li and S.-T. Lee, *J. Phys. Chem. C*, 2018, **122**, 3123–3129.
35 R. Peng, Y. d. Ma, B. b. Huang and Y. Dai, *J. Mater. Chem. A*, 2019, **7**, 603–610.
36 X. c. Ma, X. Wu, H. d. Wang and Y. Wang, *J. Mater. Chem. A*, 2018, **6**, 2295–2301.
37 Y.-L. Liu, Y. Shi, H. Yin and C.-L. Yang, *Appl. Phys. Lett.*, 2020, **117**, 063901.
38 C. f. Fu, J. y. Sun, Q. q. Luo, X. Li, W. Hu and J. Yang, *Nano Lett.*, 2018, **18**, 6312–6317.
39 D. Gu, X. m. Tao, H. m. Chen, W. l. Zhu, Y. Ouyang and Q. Peng, *Nanoscale*, 2019, **11**, 2335–2342.
40 Z. Li, L. Zhang, Y. Liu, C. Shao, Y. Gao, F. Fan, J. Wang, J. Li, J. Yan, R. Li and C. Li, *Angew. Chem.*, 2019, **132**, 945–952.
41 D. Yu, Z. Liu, J. Zhang, S. Li, Z. Zhao, L. Zhu, W. Liu, Y. Lin, H. Liu and Z. Zhang, *Nano Energy*, 2019, **58**, 695–705.
42 D. Gu, X. Tao, H. Chen, Y. Ouyang, W. Zhu, Q. Peng and Y. Du, *Phys. Status Solidi RRL*, 2019, **13**, 1800659.
43 B. J. Wang, X. H. Li, R. q. Zhao, X. Cai, W. Yu, W. Li, Z. Liu, L. Zhang and S. Ke, *J. Mater. Chem. A*, 2018, **6**, 8923–8929.
44 S. Wang, C. D. Ren, H. Y. Tian, J. Yu and M. Sun, *Phys. Chem. Chem. Phys.*, 2018, **20**, 13394–13399.
45 Y. J. Yuan, Z. j. Li, S. t. Wu, D. Chen, L. Yang, D. Cao, W. Tu, Z. Yu and Z. Zou, *Chem. Eng. J.*, 2018, **350**, 335–343.
46 R. q. Zhang, L. l. Zhang, Q. j. Zheng, P. Gao, J. Zhao and J. Yang, *J. Phys. Chem. Lett.*, 2018, **9**, 5419–5424.
47 Z. f. Zhang, Q. k. Qian, B. k. Li and K. J. Chen, *ACS Appl. Mater. Interfaces*, 2018, **10**, 17419.
48 C. F. Fu, R. Zhang, Q. Luo, X. Li and J. Yang, *J. Comput. Chem.*, 2019, **40**, 980–987.
49 R. Kumar, D. Das and A. K. Singh, *J. Catal.*, 2018, **359**, 143–150.
50 Y. Liang, J. W. Li, H. Jin, B. Huang and Y. Dai, *J. Phys. Chem. Lett.*, 2018, **9**, 2797–2802.
51 C. Long, Y. Dai, Z. R. Gong and H. Jin, *Phys. Rev. B: Condens. Matter Mater. Phys.*, 2019, **99**, 115316.
52 W. j. Yin, B. Wen, Q. x. Ge, D. Zou, Y. Xu, M. Liu, X. Wei, M. Chen and X. Fan, *Prog. Nat. Sci.: Mater. Int.*, 2019, **29**, 335–340.
53 J. Zhang, X. b. Chen, Y. Bai, C. Li, Y. Gao, R. Li and C. Li, *J. Mater. Chem. A*, 2019, **7**, 10264–10272.
54 Z. Liu, X. Yu and L. Li, *Chin. J. Catal.*, 2020, **41**, 534–549.
55 D. Ren, R. Shen, Z. Jiang, X. Lu and X. Li, *Chin. J. Catal.*, 2020, **41**, 31–40.
56 S. Shenoy and K. Tarafder, *J. Phys.: Condens. Matter*, 2020, **32**, 275501.
57 Y. J. Yuan, Z. k. Shen, S. t. Wu, Y. b. Su, L. Pei, Z. Ji, M. Ding, W. Bai, Y. Chen, Z. Yu and Z. Zou, *Appl. Catal., B*, 2019, **246**, 120–128.
58 Y. J. Yuan, P. Wang, Z. j. Li, Y. z. Wu, W. Bai, Y. Su, J. Guan, S. Wu, J. Zhong, Z. Yu and Z. Zou, *Appl. Catal., B*, 2019, **242**, 1–8.
59 Z. w. Li, J. g. Hou, B. Zhang, S. Cao, Y. Wu, Z. Gao, X. Nie and L. Sun, *Nano Energy*, 2019, **59**, 537–544.
60 D. Gu, X. m. Tao, H. m. Chen, W. l. Zhu, Y. Ouyang, Y. Du and Q. Peng, *Phys. Status Solidi RRL*, 2019, **14**, 1900582.
61 Y. Zhao, Y. He, M. Zhang and J. Shi, *J. Inorg. Mater.*, 2020, **35**, 993–998.
62 G. Kresse and J. Furthmüller, *Phys. Rev. B: Condens. Matter Mater. Phys.*, 1996, **54**, 11169–11186.
63 J. P. Perdew, K. Burke and M. Ernzerhof, *Phys. Rev. Lett.*, 1996, **77**, 3865–3868.
64 P. E. Blochl, *Phys. Rev. B: Condens. Matter Mater. Phys.*, 1994, **50**, 17953–17979.
65 A. D. Becke, *Phys. Rev. A: At., Mol., Opt. Phys.*, 1988, **38**, 3098–3100.
66 J. Klimeš, D. R. Bowler and A. Michaelides, *J. Phys.: Condens. Matter*, 2009, **22**, 022201.
67 J. Paier, M. Marsman, K. Hummer, G. Kresse, I. C. Gerber and J. G. Angyan, *J. Chem. Phys.*, 2006, **124**, 154709.
68 H. J. Monkhorst and J. D. Pack, *Phys. Rev. B: Solid State*, 1976, **13**, 5188–5192.
69 Q. Peng, Z. Y. Wang, B. S. Sa, B. Wu and Z. Sun, *Sci. Rep.*, 2016, **6**, 31994.
70 C. x. Xia, J. Du, X. w. Huang, W. Xiao, W. Xiong, T. Wang, Z. Wei, Y. Jia, J. Shi and J. Li, *Phys. Rev. B: Condens. Matter Mater. Phys.*, 2018, **97**, 115416.
71 W. Zhang and L. f. Zhang, *RSC Adv.*, 2017, **7**, 34584–34590.
72 Y. Ding, Y. l. Wang, J. Ni, L. Shi, S. Shi and W. Tang, *Phys. B*, 2011, **406**, 2254–2260.
73 T. Hu and J. M. Dong, *Phys. Chem. Chem. Phys.*, 2016, **18**, 32514–32520.
74 Y. Qun, C. j. Tan, R. s. Meng, J. Junke, L. Qiuhua, S. Xiang, Y. Daoguo and C. Xianping, *IEEE Electron Device Lett.*, 2017, **38**, 145–148.
75 B. J. Wang, X. H. Li, X. L. Cai, W. Yu, L. Zhang, R. Zhao and S. Ke, *J. Phys. Chem. C*, 2018, **122**, 7075–7080.
76 C. x. Xia, J. Du, W. q. Xiong, Y. Jia, Z. Wei and J. Li, *J. Mater. Chem. A*, 2017, **5**, 13400–13410.
77 L. Fang, Q. Feng and S. N. Luo, *J. Phys.: Condens. Matter*, 2019, **31**, 405705.
78 A. Kormányos, G. Burkard, M. Gmitra, J. Fabian, V. Zólyomi, N. D. Drummond and V. Fal'ko, *2D Materials*, 2015, **2**, 022001.